ACS OMEGA

http://pubs.acs.org/journal/acsodf

Article

Synthesis of Biogenic Hematite Nanocubes as Recyclable Dark Fenton-like Catalysts at Neutral pH and Plant Growth Applications of Degraded Waste Water

Debasmita Das, Salim Ali, Biplab Rajbanshi, Samapika Ray, Sanjoy Barman, Divya Chouhan, Md Salman Haydar, Palash Mandal, Kanak Roy, Vikas Kumar Dakua, and Mahendra Nath Roy*

Cite This: *ACS Omega* 2022, 7, 44698−44710

Read Online

ACCESS | Metrics & More | Article Recommendations | Supporting Information

ABSTRACT: The goal of this study is to fabricate bioinspired metal oxide nanocubes from lemon peel extract in an environmentally friendly manner and evaluate its impact on environmental remediation. In neutral pH, the degradation kinetics of methylene blue dye (MB) in the aqueous phase was investigated using iron oxide nanoparticles as a catalyst. The obtained results revealed that under optimum conditions, synthesized Fe_2O_3 nanoparticles (IONPs) offered ultrafast dark Fenton-like reaction to degrade MB. The size, morphological structures, and stability were confirmed through dynamic light scattering, field emission scanning electron microscopy, X-ray diffraction, and ζ potential analysis. The overall environmental impact of the process was assessed by growing wheat plants with treated wastewater and evaluating their biochemical attributes. Antibacterial activity was investigated against Gram-positive (*Bacillus megaterium*, *Bacillus subtilis*) and Gram-negative (*Escherichia coli*, *Salmonella typhimurium*) aerobics and Gram-positive cocci (*Staphylococcus aureus*). The antifungal activity was measured against *Fusarium solani* by spore germination inhibition and zone inhibition of fungal pathogens for different nanocube concentrations.

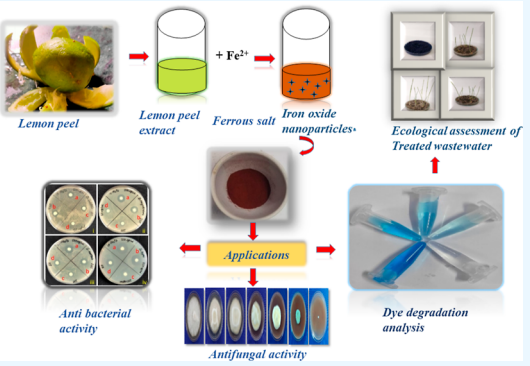

1. INTRODUCTION

With the rapid advancement of the textile industry, water pollution caused by the discharge of large volumes of industrial wastewater causes a significant environmental threat throughout the country.[1] A greater emphasis should be ascribed to textile dyes, chemicals, and huge amounts of water. Methylene blue dye (MB) is one of the cationic dyes, used primarily in the textile, rubber, paper, cosmetic, and printing industries. It can be also used for pharmaceutical purposes. Because of its carcinogenic, mutagenic, and non-biodegradable properties, it is designated as a hazardous dye. Its indirect effects on human health include hyperactivity in children, bladder cancer, and allergic reactions and may be responsible for eye burn.[2] The aromatic rings and polar groups of the dye structure resist complete degradation of the dye. The most commonly used technique for degrading these dyes is oxidation.[3,4] Several environmentally friendly and cost-effective oxidants, such as manganese oxide, ozone, and hydrogen peroxide, can be used for the dye degradation.[5] The Fenton reaction system combines ferrous ions and hydrogen peroxide, whereas the Fenton-like reaction system combines hydrogen peroxide and iron species but does not include ferrous ions. Because they require iron species rather than ferrous ions, Fenton-like reactions have several advantages over Fenton reactions.[6] In addition, Fenton reaction systems require an acidic medium. So, their operation in an acidic medium imposed certain constraints, such as metal leaching and sludge formation, while advocating for green and sustainable environmental aspects. Previous reports had also agreed on this point.[7−9] Yang et al. investigated the degradation of MB in the presence of magnetic nanoparticles in acidic pH using the Fenton reaction.[10] Therefore, this research work has focused on developing a Fenton reagent that works in neutral pH to overcome the aforementioned drawbacks. Another significant issue is that the textile industry consumes a large amount of water; as a result, the amount of wastewater (containing organic pollutants) generated in the dyeing and finishing processes is also large and should be recycled. Detoxification of organic contaminants such as textile dyes is critical for both water purification and reusability. In this regard, we examined the growth of wheat plants before and after degradation of dye-contaminated water, and to ensure the quality of degraded wastewater, the biochemical quality of the wheat plant was monitored.

Received: June 17, 2022
Accepted: October 21, 2022
Published: December 1, 2022

Green chemistry has yielded a range of nanomaterials that may be better alternatives for traditional antibacterial and antifungal agents. Phytosynthesis of Fe_2O_3 nanoparticles (IONPs) from *Avicennia marina*,[11] *Ficus carica*,[12] *Sapindus mukorossi*,[13] *Lagenaria siceraria*,[14] *Kappaphycus alvarezii*,[15] *Amaranthus spinosus*,[16] *Daphne mezereum*,[17] *Citrus maxima*,[18] and *Cymbopogon citratu*[19] have been mentioned in the previous works. Commercially, 34% of lemons produced each year are ingested for juice production, resulting in about 44% of peel waste, causing a huge issue for processing industries.[20] As lemon peel contains a high concentration of active phytochemicals, it may be a better alternative for IONPs synthesis.[21] Previous research has discovered that biomediated IONPs have bactericidal effects against both Gram-positive and Gram-negative bacteria.[22,23] In addition to bactericidal effects, hematite NPs also exhibit notable antifungal properties.[24−26] In the present study, antifungal activity was analyzed against *Fusarium solani* (*F. solani*) by both qualitative and quantitative methods.

The main objectives of our recent work are (a) to synthesize IONPs in an environmentally friendly manner, (b) to evaluate the antimicrobial activity of green-mediated NPs against biological pollutants, (c) to assess antioxidant activity, (d) to assess catalytic activity via a Fenton-like process at neutral pH, and (e) to assess the efficacy of dye-degraded water for seed germination studies. For the first time, the efficiency of hematite nanocubes as heterogeneous Fenton-like catalysts for MB dye degradation has been studied at neutral pH and in dark conditions.

2. MATERIALS AND METHODS

2.1. Materials. Ferrous sulfate ($FeSO_4$, $7H_2O$) salt (99.99%), hydrogen peroxide (H_2O_2) (99.99%), and MB dye (99.99%) were procured from Himedia, India. The aqueous solution of MB was considered as model wastewater. The Sonalika cultivar of wheat was collected from the National Seed Corporation of India, Pvt. Ltd.

2.2. Preparation of *Citrus limon* Peel Extract. *Citrus limon* was first collected from the campus of North Bengal University in West Bengal, India. Manually removed peels were washed and chopped into homogeneous species (length: 0.5 ± 0.04 cm, thickness: 4 ± 0.05 cm). 50 g of peel was sonicated in 250 mL of water and heated for 1 h at 70 °C. The peel extract was refrigerated after being filtered through Whatman 40 filter paper (Merck, Germany).

2.3. Biosynthesis of IONPs. The standard procedure was developed by previous authors for the biosynthesis of metal oxide nanoparticles used with minor modifications.[27] 5 g of ferrous sulfate salt was added to 100 mL of peel extract, and pH was maintained at 11 by using 2 N NaOH solution. The mixture was heated for 2 h at 75 °C under stirring conditions. The solution changed its color from light green to dark brown. To collect the pallet of IONPs, the solution was centrifuged at 10,000 rpm for 10 min. The pallet was then washed and dried at 70 °C. The obtained product was annealed at 400 °C and stored in a glass vial.

2.4. Phytochemical Screening of *Citrus limon* Peel Extract. *Citrus limon* peel extract (LPE) was phytochemically analyzed to confirm the active constituents responsible for NPs formation. It was carried out following a standard method.[28] These phytoconstituents act as reducing and stabilizing agents during the synthesis of IONPs (Table S1).

2.5. Determination of Optimum Conditions for the Removal of Organic Dyestuff by Fenton-like Reaction. The Fenton-like oxidation process is advantageous over the other techniques to degrade the organic contaminants, and it is also cost-effective. At room temperature, the catalytic activity of IONPs was measured against MB dye (10 mg/L) in the dark. In this Fenton-like reaction, pH, nanocatalyst amount, and H_2O_2 concentration were investigated to determine the optimum conditions. The reaction mixture was exposed to UV light to measure the absorbance at 664 nm. Similarly, 665 nm is considered as an absorbance peak for MB in another work.[29] After specific time intervals, the sample (2 mL) was withdrawn and the percentage of degradation was calculated using eq 1:

$$\%\ \text{degradation} = \left(\frac{C_0 - C_t}{C_0}\right) \times 100 \tag{1}$$

where C_0 and C_t are the actual concentration of MB in mg/L and the remaining concentration of MB after time t, respectively.

The rate of degradation of MB dye was monitored by the pseudo-first-order reaction model (eq 2):

$$\ln(C_t/C_0) = -k_1 t \tag{2}$$

where k_1 is the pseudo-first-order rate constant (min^{-1}). The slope of the plot yields the rate constant value of respective reactions.[30]

2.6. Analysis of Effect of the Treated Wastewater on Plant Growth. Wheat seed germination time and seedling vigor index were determined to investigate the effect of degraded wastewater on plant growth. For the experiment, healthy seeds of uniform size were chosen. Seeds were thoroughly washed with distilled water before being sown into Petri plates containing 100 g of sand mixed with the required samples. Each plate contained 10 seeds. The NPs solution (control), distilled water (control), treated wastewater, and dye solution were used to treat the seeds. Seedlings were left to grow for 10 days and regularly watered (Figure 5a−d). The following germination parameters were evaluated (eqs 3−6):

$$\text{germination index} = \sum (G_t/T_t) \tag{3}$$

where G_t is the number of seeds germinated on the tth day and T_t is the number of days up to the tth day;

$$\text{mean germination time} = \frac{\sum (d \times n)}{\sum n} \tag{4}$$

where n is the number of seeds germinated on day d and d is the number of days counted from the beginning of germination;

$$\text{coefficient of velocity} = \left(\frac{\sum N_i}{\sum N_i T_i}\right) \times 100 \tag{5}$$

where N is the number of seeds germinated on day i and T is the number of days from sowing; and

$$\text{promptness index} = (N_t 2 \times 1) + (N_t 3 \times 0.67) + (N_t 4 \times 0.33) \tag{6}$$

where N_t is the number of seeds germinated on the t th day.

2.7. Evaluation of Biochemical Attributes of Treated Wheat Seedlings. *2.7.1. Estimation of Total Phenol.* Total

https://doi.org/10.1021/acsomega.2c03798
ACS Omega 2022, 7, 44698−44710

phenols were extracted from 1 g of fresh tissue homogenized in 2 mL of 90% methanol. The extract was centrifuged at room temperature for 8 min at 10,000 rpm. Then the supernatant was collected and used for estimation. 1 mL of methanolic extract was mixed with the same amount of 95% ethanol. 0.5 mL of 50% Folin-Ciocalteu was added and incubated at room temperature for 5 min. After incubation, 1 mL of 5% Na_2CO_3 was added to the reaction mixture and incubated for another hour. The absorbance of the navy-blue reaction mixture was measured on a spectrophotometer at 725 nm (Systronics 169). Gallic acid was used as a standard to calculate the total phenol.

2.7.2. Estimation of Ortho-Dihydric Phenol. The extract was made exactly as described in the phenol estimation. The total phenol content was estimated by following Malick and Singh.[31] 0.5 mL of methanolic extract was mixed with 0.5 mL of 0.5 N HCl. The reaction mixture was vortexed after the addition of Arnow's reagent. Then 1 mL of 1 N NaOH was added to it and thoroughly mixed until a pink color appeared. On a spectrophotometer, the absorbance of the reaction mixture was measured at 515 nm. Catechol (1000 μg/mL) was used as a standard.

2.7.3. Estimation of Flavonoid Content. 0.1 mL of methanolic extract was combined with 0.3 mL of 5% $NaNO_2$. After 5 min, 0.3 mL of 10% $AlCl_3$ was added and incubated for another 6 min. After that, 2 mL of 1 N NaOH was added to the prior solution. A light-orange color appeared, with an absorbance of 510 nm. For the estimation of flavonoid content, quercetin was used as a standard.

2.7.4. Estimation of Total Reducing Sugar. Reducing sugar was calculated by employing the Miller method (1972). The laboratory-prepared methanolic extract (1 mL) of the seedling was evaporated and reconstituted with the same amount of water. 1 mL of dinitro salicylic acid (DNSA) reagent was added. The solution was incubated in a water bath for 5 min. Then 1 mL of 40% Rochelle salt solution was added and a deep reddish yellow color developed. The absorbance was measured at 510 nm. The maltose standard curve was used to estimate the total reducing sugar.

2.7.5. Estimation of Total Chlorophyll. 1 g of fresh tissue was weighed and crushed in a mortar and pestle with 20 mL of 80% acetone. The extract was centrifuged at room temperature for 8 min at 10,000 rpm. Then the supernatant was collected and the absorbance was measured (Arnon, 1949).

2.8. Antioxidant Activity. The DPPH free-radical scavenging assay was used to assess the antioxidant activity, which was expressed in terms of IC_{50} value. It is the theoretical concentration of samples where 50% of the radical is scavenged. Various concentrations of tested samples were reacted with DPPH solutions (500 μL). For the reference standard, ascorbic acid was used in the same concentration. The solution was kept in the dark. After incubation for 30 min, absorbance was measured at 517 nm using a UV−vis spectrophotometer and % of inhibition was measured according to eq 7:

$$\%\ \text{inhibition} = \left(\frac{A_0 - A_1}{A_0}\right) \times 100 \tag{7}$$

where A_0 and A_1 are the absorbances of control and tested samples, respectively.

2.9. Antibacterial Activity. The target microorganisms chosen for the antibacterial activity were *Bacillus megaterium* (*B. megaterium*) ATCC 14,581; *Bacillus Subtilis* (*B. subtilis*) ATCC 11,774; *Staphylococcus aureus* (*S. aureus*) ATCC 11,632; *Escherichia coli* (*E. coli*) ATCC 11,229; and *Salmonella typhimurium* ATCC 25,241.[31] An actively dividing test organism (300 μL) was then added to the nutrient agar plate. The plates were allowed to solidify, and after that, different concentrations of IONPs-soaked paper discs were placed on the plate surface. The bactericidal activity of the studied sample was evaluated in terms of zone of inhibition (measured around the disc using the mm scale) and minimum inhibitory concentration (MIC). For that, 100 μL of the studied microorganism was added to 30 mL of sterilized nutrient broth and maintained at 10^6 CFU/mL. After 24 h of incubation, microbial growth was evaluated by taking absorbance at 600 nm using a Systronics Spectrophotometer-2201.

2.10. Antifungal Activity. *2.10.1. Antifungal Activity of IONPs on Fusarium solani Radial Mycelium Growth.* The antifungal activity of IONPs was investigated by the poisoned food assay.[32] Different concentration ranges of NPs were prepared and sterilized at 121 °C and 15 lb/inch^2 pressure for 15 min. NPs were mixed up with sterilized potato dextrose agar (PDA) media and poured into a 90 mm Petri dish. A 0.5 cm mycelium disc, excised from 7 days old culture, was placed at the center of each plate. A plate without any NPs treatment was prepared for comparison. Treatment plates were incubated for 7 days at 27 °C. The efficiency of the NPs against fungal mycelium growth was calculated by percentage inhibition of radial growth (PIRG) (eq 8):

$$\text{PIRG} = \left(1 - \frac{R_2}{R_1}\right) \times 100 \tag{8}$$

where R_1 represents colony growth in the control plate and R_2 represents radial growth of the colony in the treated plate.

2.10.2. Effect of IONPs on F. solani Spore Germination Inhibition. *F. solani* spore suspension was made by pouring 10 mL of sterilized distilled water into sporulated culture tubes that had been incubated for 7 days. The tubes were shaken gently and scratched with a sterilized needle. 1×10^6 conidia/mL were present in the spore suspension. 10 L of the spore suspension was mixed with equal parts of various concentrations of IONPs. The hybrid was incubated at 27 °C for 6 h. After incubation, the hybrid was treated with cotton blue and viewed under a light microscope. The total number of germinated spores was counted in microscopic fields that were chosen at random. The percentage of spore germination inhibition (% SGI) was calculated as follows (eq 9):[33]

$$\%\ \text{SGI} = \left(\frac{N_{\text{GS,control}} - N_{\text{GS,treatment}}}{N_{\text{GS,control}}}\right) \times 100 \tag{9}$$

3. PHYSICAL CHARACTERIZATION

The pure phase of Fe_2O_3 nanocube was revealed using various characterization techniques such as Fourier transform infrared spectroscopy (FTIR), FE-SEM, X-ray diffraction (XRD), and UV−vis spectroscopy. A Perkin Elmer Spectrum 2 was used to detect the role of phytochemicals in metal ion reduction and stabilization. The purity and size of NPs were determined using an X-ray diffractometer (Bruker D8 Advance). UV−vis spectroscopy was used to identify the characteristic surface plasma resonance (Perkin Elmer Lamba 35). The morphological data were collected by FE-SEM (JEOL JSM-7610F

https://doi.org/10.1021/acsomega.2c03798
ACS Omega 2022, 7, 44698−44710

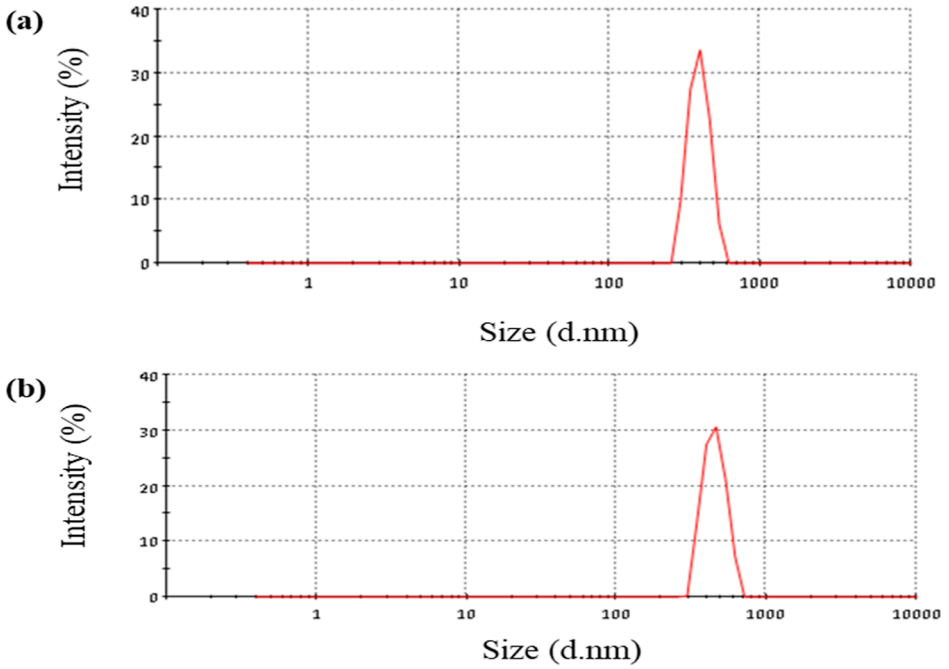

Figure 1. DLS study IONPs (a) after synthesis and (b) 200 days.

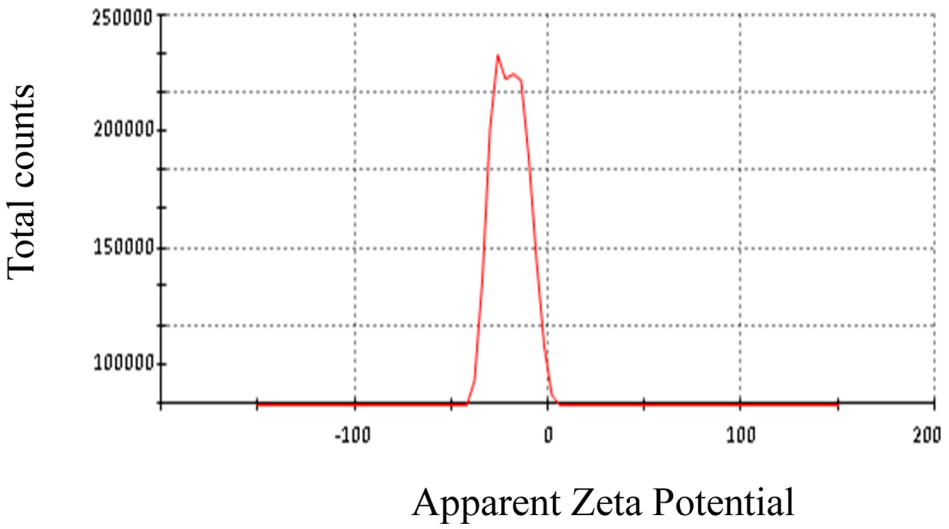

Figure 2. ζ potential of synthesized IONPs.

Plus) analysis, and the various morphological changes on the fungal conidia as a result of different treatments were observed using SEM (JSM-IT 100; JEOL). ζ potential analyzer confirmed the stability of bioinspired IONPs (Malvern Zetasizer Nano ZS90).

4. RESULTS AND DISCUSSION

4.1. Dynamic Light Scattering. Dynamic light scattering (DLS) was used to determine the size of the NPs (Figure 1a). The polydispersity index of the synthesized nanocubes was found to be 0.332, indicating their monodisperse nature. The sharpness of the peak also reflected the cubical shape of NPs. DLS study was repeated after 200 days, and it was found that the size and polydispersity index (0.334) did not deviate much, reflecting their stability (Figure 1b). The size determined by DLS is larger than the size determined by FE-SEM, caused by cluster formation.[34]

4.2. ζ Potential Analysis. ζ potential analysis was used to determine the stability and surface charge of biosynthesized NPs (Figure 2). A lower ζ potential value implies that the NPs are more stable as they repel each other when attempting to aggregate. The slightly negative charge on the surface of the NPs provides stability when stored for more than a month. The threshold value of electrostatic stabilization is −19.6 mV, which can be attributed to the −COOH and −OH groups of LPE. Higher ionization in an alkaline medium leads to ionized species and, as a result, increased repulsion from negatively charged species, resulting in colloidal stability.[35,36]

4.3. UV−Vis Spectroscopy. Different spectroscopic techniques were used to describe the nanocubes' formation (Figure 3). Table 1 compares the UV absorption data of synthesized NPs with the previous works. UV−visible spectroscopy is the most reliable technique to establish the fact of the formation of NPs. The transition of valance bond

https://doi.org/10.1021/acsomega.2c03798
ACS Omega 2022, 7, 44698−44710

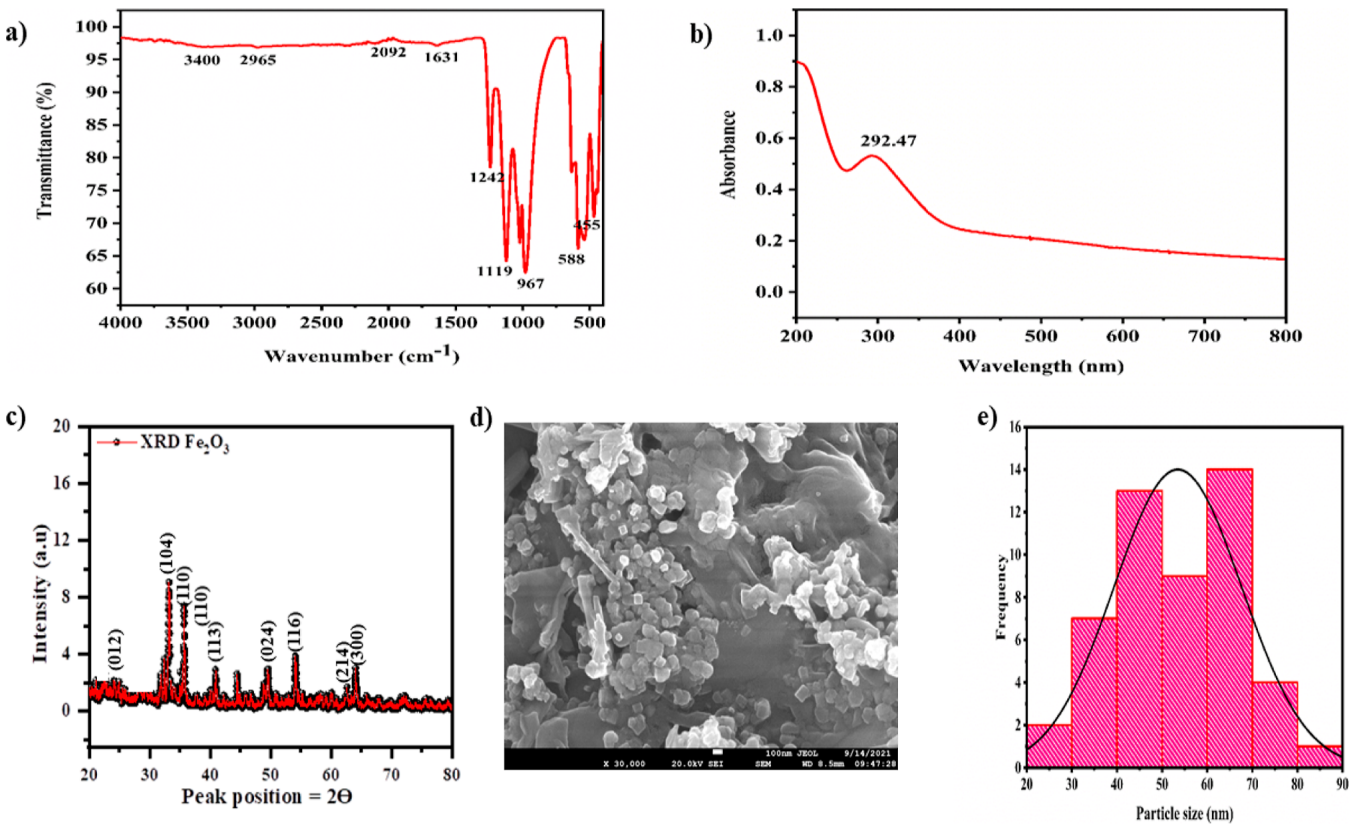

Figure 3. (a) ATR-FTIR spectra, (b) UV−visible optical absorption maximum, (c) XRD spectra, (d) morphology picture (FESEM), and (e) particle size distribution histogram of IONPs.

Table 1. UV Absorption Statistics of Iron Oxide Nanoparticles Compared to the Literature

UV absorption (nm)	synthesis methods
272	precipitation[39]
250	sol−gel[40]
459	*Moringa oleifera*[41]
238	sol−gel[42]
390	co-precipitation[43]
380−540	microemulsion[44]
292	this work

electrons to the conduction band causes surface plasma resonance at 292 nm[37] (Figure 3b). The broadening of the peak indicates the polydispersed nature of NPs.[38] Figure 3b represents the UV−vis spectra of synthesized NPs.

4.4. Fourier Transform Infrared Spectroscopy. FTIR spectra revealed that the functional groups were responsible for the stabilization and reduction of IONPs (Figure 3a). The absorption bands near 588, 455, and 967 cm^{-1} indicate the clear formation of IONPs.[22,45,46] The wide range of bands corresponding to 3300−3400 cm^{-1} stand for O−H groups coming from polyphenolic compounds.[47,48] The amplitude of the peak at 967 cm^{-1} corresponds to the bending vibration of alkenes. Carbonyl stretching mode was reflected by the band at 1631 cm^{-1}.[49] The bands at 2965 cm^{-1} can be considered for carboxylic acid. Bands corresponding to 1119 cm^{-1} appear for C−O stretching of alcoholic compounds.[50] O−H bending vibration is reflected by 1631 cm^{-1}.[51] Bands at 1242 and 1631 cm^{-1} showed absorption stretch of COO− and amide I bonds, respectively.[52] The vibrational bands corresponding to 577 cm^{-1} appeared due to intrinsic stretching vibrations of the metal at the tetrahedral site, whereas 455 cm^{-1} appeared for vibrations of the metal at an octahedral site.[53,54] The bands corresponding to −C−O−C, C═C, O−H, and −C−O appear from flavonoids, polyphenols, and alkaloids present in LPE.[22] Figure S1 explains the role of phytochemicals in LPE as reducing and stabilizing agents. These phytochemicals remain attached to the synthesized NPs even after high thermal annealing at 400 °C.[47]

4.5. Morphological Characterization of IONPs. FE-SEM provides a clearer picture than conventional SEM with 3−5 times better resolution.[55] Figure 3d reflected the cubical shape of synthesized IONPs with an average size in the range of 40−70 nm (Figure 3e). In previous research work, cubical iron oxide NPs were prepared by the sonochemical method with sizes in the micrometer range.[56]

4.6. X-Ray Diffraction. The XRD pattern of biosynthesized nanocubes is depicted in Figure 3c. The primary peaks were seen at 24.49°, 33.22°, 35.71°, 40.93°, 49.55°, and 54.14° with the miller indices of (012), (104), (110), (113), (024), and (116), respectively. These data are also in agreement with the literature (JCPDS no: 33-0664).[57,58] The peaks at 33.22° (104) and 40.93° (113) are solely of Fe_2O_3 structure. The sharp peaks also indicate the high crystallinity of NPs. The crystal size (D), dislocation density (δ), and microstrain (ε) were calculated using eqs 10−12:

$$D = \frac{0.9\lambda}{\beta \cos \theta} \tag{10}$$

$$\delta = \frac{1}{D^2} \tag{11}$$

https://doi.org/10.1021/acsomega.2c03798
ACS Omega 2022, 7, 44698−44710

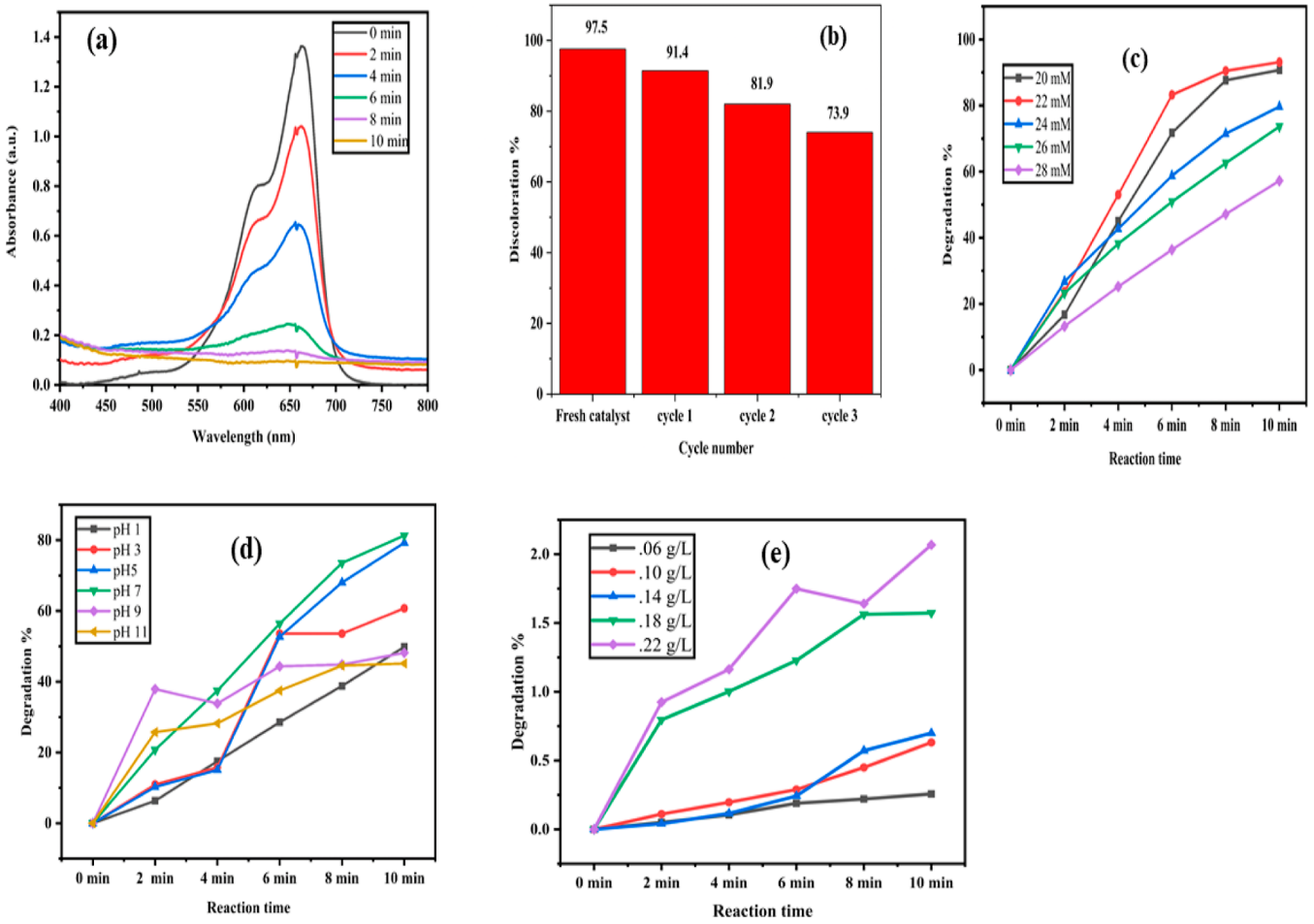

Figure 4. Fenton-like reactions of MB dye in the presence of the nanocatalyst: (a) UV−vis absorption spectra of MB degrading using IONPs, (b) effect of recycling the catalyst on MB removal catalytic cycles of degradation of MB, (c) effect of concentration of H_2O_2 with a fixed amount of catalyst and at constant pH on Fenton-like reaction rate, (d) effect of pH on the rate of Fenton-like reaction at a constant amount of H_2O_2 and nanocatalyst, and (e) effect of concentration of catalyst with a fixed amount of H_2O_2 and at fixed pH on Fenton-like reaction rate.

$$\varepsilon = \frac{\beta \cos \theta}{4} \tag{12}$$

where D is the size of the particle, λ is the wavelength of X-rays (1.5406 Å), θ is the Bragg angle for the peak, and pure diffraction broadening is designated by β. The value of k is taken as 0.9. The average crystalline size was found to be 42 nm. Table S2 reflects the XRD data of synthesized NPs. However, the previous research found that the average crystal size was 24 nm,[27] 60 nm,[59] 41.5 nm,[60] 21 nm, and 39 nm.[61] Smaller crystallite sizes result in larger dislocation densities, indicating an inverse relationship between size and density. The data table shows that the synthesized NPs have compressive strain (all values are positive), which can be attributed to the oxygen vacancies.[62] Previous research reported a value of 2.011 for microstrain.[63]

4.7. Removal of Methylene Blue. The finest wavelength for dyestuffs was determined at 664 nm, and this wavelength was used for optimization studies at room temperature. Prior work also found the optical density at 664 nm for the photocatalytic reaction.[64] pH plays a crucial role in this heterogeneous Fenton-like reaction. Temperature also plays a vital role as a small change in temperature can change the equilibrium position of this chemical process.[65] Here, 97% of the dye is degraded in 10 min (Figure 4a).

4.7.1. Method Optimization for Dye Removal via Fenton-like Reaction. 4.7.1.1. Determination of Optimal Nano-bio-catalyst Amount. To evaluate the influence of the catalyst concentration on Fenton-like reactions, different concentrations of the biocatalyst were utilized. The dosage ranged from 0.06 to 0.22 g/L (Figure 4e). The various amounts of nanocatalyst were weighed in an analytical balance before being placed in 30 mL of 10 mg/L MB solution at constant pH 7 and a fixed amount of 22 mM H_2O_2. The rate of degradation increases with increasing nano-bio-catalyst concentration and reaches the peak efficiency at 0.22 g/L (degradation percentage = 97.5) in 10 min (Figure 4e). Other studies showed that IONPs with a concentration of 1 and 2.5 mg/L have the highest degradation efficiency.[66,67] The number of active sites increases as the catalyst dose increases, resulting in a significant number of hydroxyl radicals attacking the methylene blue chromophore groups. The oxidation reaction is also aided by the catalyst's high surface contact availability.[68] Figures S2c and S3a show that the value of the rate constant increases as the amount of nanocatalyst increases and that under optimum conditions, it has the highest rate constant value (R^2 = 0.95).

4.7.1.2. Determination of Optimal pH. The pH was varied from 1 to 11 to see how it affected the dark Fenton-like system at a fixed amount of H_2O_2 (22 mM) and nanocatalyst (0.22 g/

https://doi.org/10.1021/acsomega.2c03798
ACS Omega 2022, 7, 44698−44710

L). The conclusion was that pH 7 provided the best result for maximum dye degradation from wastewater and thereby solved the problem of the higher acidic medium of Fenton reaction systems. After pH 7, degradation becomes slow. This is due to the fact that at higher pH levels, the Fe^{3+} ions react with peroxide to produce H_2O and O_2 rather than active $OH^•$ radicals. Abhilasha et al.[69] showed that the optimum pH for dye removal is 3. However, Ayodamope proposed that a suitable pH range is 2−4.[66] In the low pH range (pH < 2), the degradation process becomes slow due to rapid corrosion of IONPs (Figure 4d). The linear plot indicates that MB dye degradation follows pseudo-first-order kinetics (Figure S2b). Figure S3b shows that the value of the pseudo-first-order rate constant was maximum at pH 7 (R^2 = 0.9872) and shows a decreasing trend in an alkaline medium.

4.7.1.3. Determination of Optimum Peroxide Concentration. The effect of hydrogen peroxide on dye degradation was investigated at different concentrations ranging from 20 mM to 28 mM while keeping the amount of nanocatalyst (0.22 g/L) and pH (pH = 7) constant (Figure 4c). When 20 mM peroxide was added to the reaction medium, 89% of the dye was degraded, and when 22 mM peroxide was used, 93% of the dye was degraded. For the highest concentration of peroxide, the degradation percentage is 57%. Therefore, the maximum efficiency was found at 22 mM concentration of H_2O_2. In the previous work, 130 μL (30%) of hydrogen peroxide was used for the degradation of MB dye.[69] The determination of the optimum peroxide concentration is required from a commercial standpoint as well as to avoid toxicity. At low concentrations, peroxide attacks the aromatic ring of organic pollutants, whereas at high concentrations, peroxide acts as a scavenger for highly potent $OH^•$ radical, producing $HO_2^•$ radical with a lower oxidation potential E_0 ($HO_2^•/H_2O$) = 1.7 V and E_0 $HO^•/H_2O$ = 2.8 V and decreasing the efficiency of the Fe^{3+}/H_2O_2 moiety to perform the catalytic reaction.[66,70,71] $HO_2^•$ combines with $HO^•$ causing the destruction of $HO^•$ as shown in eqs 13 and 14

$$H_2O_2 + HO^• \rightleftarrows HO_2^• + H_2O \quad (13)$$

$$HO^• + HO_2^• \rightleftarrows H_2O + O_2 \quad (14)$$

The value of the pseudo-first-order rate constant first increases up to 22 mM H_2O_2 and then decreases. A linear plot was made to eq 2. These plots are demonstrated in Figure S2a, and this first-order plot illustrates good linearity. The R^2 value of the first-order rate equation is 0.9703 and the degradation constant is 0.3387 min^{-1} at an optimum concentration of H_2O_2 (Figure S3c).

4.7.1.4. Regeneration Recycling Study. Aside from degradation efficiency, the recycling ability of the nanocatalyst was investigated to determine the long-term viability of the proposed process. The reusability was tested up to three cycles, as shown in Figure 4b. An external magnetic field was used to recover IONPs, which were then washed with water and ethanol.[72] The washed NPs were then dried at 80 °C for future use. After the third cycle, recovered NPs have nearly the same size (as measured by DLS in Figure S11) and stability (ζ Potential as shown in Figure S12). There is only a ∼24% reduction in degradation efficiency after the third cycle, which may be due to material loss during recycling.[73] The same conditions were maintained for all the cycles.

4.7.1.5. Possible Mechanism of Methylene Blue Dye Degradation via Fenton-like Reaction. The rapidity of the degradation process can be claimed by Fe^{3+} of Fe_2O_3. In this catalytic degradation process, Fe^{3+} forms $OH^•$ by surface absorption of H_2O_2 and degrades into ferrous ions, hydroperoxyl radicals, and hydrogen ions according to eqs 15−19. Then ferrous ions are converted into ferric ions along with generation of OH^- and $OH^•$. This $OH^•$ plays the main role in degradation of MB to give non-toxic products. A similar mechanism is also demonstrated by previous work for degradation of crystal violet dye by Fe_2O_3 nanocubes[27,74]

$$Fe(III) + H_2O_2 \rightarrow Fe(II) + HO_2^• + H^+ \quad (15)$$

$$Fe(II) + H_2O_2 \rightarrow Fe(III) + OH^• + OH^- \quad (16)$$

$$HO_2^• + Fe(III) \rightarrow Fe(II) + O_2 + H^+ \quad (17)$$

$$OOH^• + Fe(II) \rightarrow Fe(III) + HO_2^- \quad (18)$$

$$H_2O_2 + OH^• \rightarrow HO_2^• + H_2O \quad (19)$$

4.7.2. Comparison with the Literature. Table 2 compares the catalytic performance of Fe_2O_3 NPs to the literature in order to assess the relevance of the current work. In terms of catalytic dosage, reaction conditions, and reaction time, our synthesized NPs have a higher degradation efficiency than previous work. In 10 min, 97% of the dye is degraded (Figure 4a). This catalyst is completely environmentally friendly and operates in the dark at neutral pH, overcoming the dependency of UV light and the acidic medium to simplify the complexities of the photo Fenton reaction.

Table 2. Comparative Study of Catalytic Activity of Fe_2O_3 NPs against Degradation

catalyst	MB degradation (%)	reaction time	ref
Fe_2O_3 NPs	97	10 min	this work
iron-oxide-containing graphene/carbon nanotube	99	60 min	75
PB-modified iron oxide NPs	100	120 min	76
carbon-doped Fe_2O_3 NPs	96	420 min	77
Ba−Cu-based M-hexaferrite NPs	98−99	120 min	78
cobalt ferrite magnetic NPs	80	140 min	79
FeO−Fe_3O_4-RGO	98	60 min	80
iron oxide/graphene hybrid nanomaterials	>99	60 min	81
henna leaf-mediated iron oxide NPs	95	50 min	82
Fe_2O_3 NPs	97	30 min	83
iron NPs synthesized using *Galinsoga parviflora*	92	40 min	84
leaf-assisted Fe_2O_3 NPs	69	2 h	41

4.8. Treated Wastewater for the Growth of Seed Germination. A simple bioassay was performed to ensure the practicability and viability of degraded wastewater for reuse.[85] Because the quality of treated wastewater is thought to be lower than that of standard irrigation water, it is thought to inhibit wheat seed growth, but the reality is different.[86] Wheat seeds were fed with distilled water (control), the NP solution (control), treated wastewater, and the dye solution in a separate manner.[87] The germination index of seedlings treated with NPs was found to be higher than that of seedlings treated with treated wastewater and distilled water. The seedlings treated with MB had a low germination rate, resulting in the

https://doi.org/10.1021/acsomega.2c03798
ACS Omega 2022, 7, 44698−44710

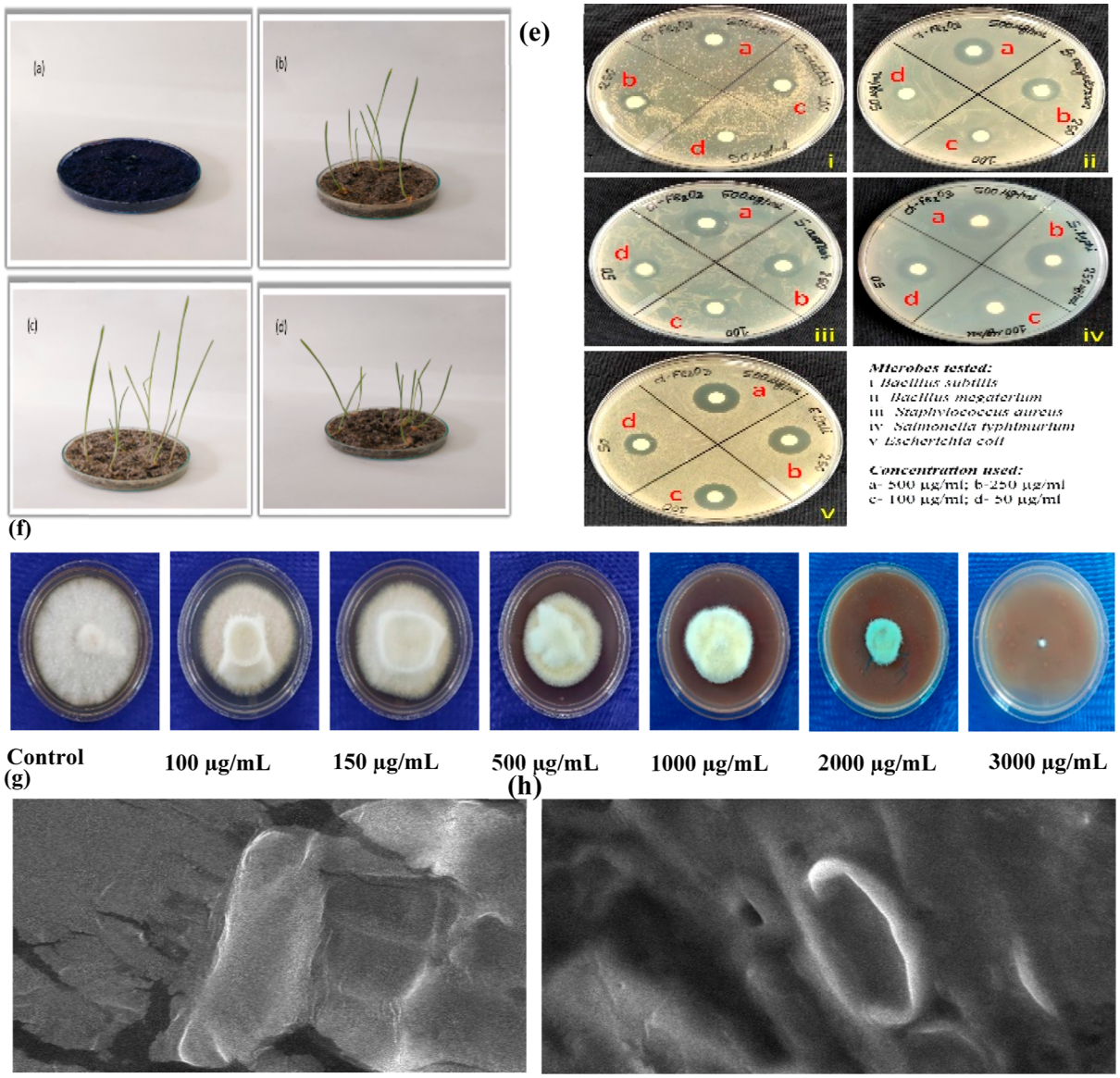

Figure 5. (a) Seeds treated with dye water; (b) seeds treated with distilled water (control); (c) seeds treated with IONP solution (control); (d) seeds treated with degraded wastewater; (e) enhanced antibacterial activity of IONPs synthesized form LPE; (f) antifungal activity of IONPs at different concentrations against *F. solani* after 10 days of incubation; (g) ultrastructural changes of fungal conidia observed under a scanning electron microscope: untreated conidia and (h) NPs (3000 μg/mL)-treated conidia.

lowest germination index. The mean germination time of NP-treated seedlings was found to be the shortest of all treatments, while seedlings treated with treated wastewater had a slightly higher mean germination time than NPs-treated seedlings. Seedlings treated with distilled water and MB, on the other hand, had the shortest mean germination time. Similarly, the coefficient of the velocity of germination was found to be the highest in the NPs-treated seedlings and the lowest in the MB-treated seedlings (Figure S4). These results show that treated wastewater can be used safely for plant growth. However, more research is required for edible plants. This technique can help to limit the overuse of natural water and promote the reuse of treated wastewater for non-edible irrigation.[73]

4.9. Evaluation of Biochemical Attributes of Wheat Seedlings Treated with Degraded Wastewater. The results inform us that treated wastewater has a higher potential to improve physiological parameters as compared to distilled water (control) and non-degraded water. The phenol content was found to be higher in the case of NPs-treated seedlings. Seedlings that were treated with wastewater also showed elevated phenol content next to NPs-treated seedlings. Distilled water-treated seedlings showed moderate phenol content in them. The phenol level of seedlings treated with MB dye was insignificant. Similar results were obtained in the case of ortho-dihydric phenol, flavonoid, total chlorophyll, and reducing sugar content estimation (Figure S5). Therefore, it can be concluded that degraded water after centrifugation maintains the ecological balance.

4.10. In Vitro Antioxidant Activity. Figure S8 depicts the antioxidant activity of IONPs. The surface reaction between IONPs and 1,1-diphenyl-2-picrylhydrazyl radicals (generated by the transfer of electrons) is responsible for antioxidant activity.[88] In this case, the concentration of the antioxidant ranged from 50 to 800 μg/mL. The highest level of radical inhibition (72.73%) was observed at the highest concentration of NPs (800 μg/mL), with an IC_{50} value of 421.03 μg/mL.

https://doi.org/10.1021/acsomega.2c03798
ACS Omega 2022, 7, 44698−44710

Table 3. Zone of Inhibition of the IONPs against Gram-Positive and Gram-Negative Bacterial Strains

	zone of inhibition (in mm)			
microbes tested	50 μg/mL	100 μg/mL	250 μg/mL	500 μg/mL
B. subtilis	6.333 ± 0.577	8 ± 1	9.333 ± 0.577	10.667 ± 0.577
B. megaterium	5.667 ± 0.577	7.667 ± 1.155	12 ± 1	13.667 ± 0.577
S. aureus	8.667 ± 0.577	9 ± 1	11.667 ± 0.577	14.333 ± 0.577
S. typhimurium	11.333 ± 0.577	14.667 ± 0.577	17 ± 1	18.667 ± 0.577
E. coli	10.333 ± 0.577	13.667 ± 0.577	13.667 ± 0.577	15 ± 0.577

Therefore, the IC_{50} value admitted that IONPs showed dose-dependent antioxidant activity. Previous research has yielded similar results.[89] There is some disagreement in the literature regarding the antioxidant activity of IONPs; in some cases, NPs outperformed ascorbic acid, while in others, ascorbic acid outperformed NPs.

4.11. Antimicrobial Activity. Significant growth inhibition by the disc diffusion method was found for the lowest (50 μg/mL) and highest concentrations (500 μg/mL) of IONPs, as shown in Figure 5e and Table 3. However, *B. subtilis* growth inhibition is insignificant at lower (6.33 ± 0.58 mm) and higher (10.67 ± 0.58 mm) IONPs concentrations. *B. megaterium*, *S. aureus*, and *E. coli* yielded inconclusive results. The data are shown in Figure S6. Growth inhibitory activity of synthesized NPs is found to be lower for Gram-positive bacteria, resulting in higher MIC values for Gram-positive bacteria.[90] The MIC value for Gram-positive cocci like *S. aureus* was 160 μg/mL, and that for Gram-negative bacteria like *E. coli* was found to be 140 μg/mL (Table 4). The possible

Table 4. MIC Values of Biosynthesized IONPs against Gram-Negative and Gram-Positive Bacterial Strains

minimum inhibitory concentration (μg/mL)				
B. subtilis	*B. megaterium*	*S. aureus*	*S. typhimurium*	*E. coli*
280	200	160	120	140

mechanism of antibacterial activity was demonstrated in Figure S7. Previous studies have shown that chemically synthesized Fe_2O_3 NPs have better antibacterial activity against *Shigella dysenteriae* (inhibition zone 11 mm, at a concentration of 150 g/mL).[91] IONPs synthesized by the co-precipitation method showed good antibacterial activity at a low concentration against *B. subtilis* and *E. coli*,[92] and green synthesized IONPs showed antibacterial activity at a concentration of 30 μg/mL.[93]

4.12. Antifungal Activity. Figure 5f shows the antifungal activity of the synthesized NPs. A concentration of 3000 μg/mL results in complete inhibition. Khatami et al. admitted that at a concentration of 25 μg/mL, *Rhizoctonia solani* growth inhibition was 83%,[94] whereas biomediated silver NPs showed 83% growth inhibition against *F. solani*.[95] Also, silver-doped TiO_2 NPs showed a good performance against these fungi.[96] Scientists believe that NPs work by inhibiting replication and growth of fungi by deactivating the DNA enzyme. However, the complete mechanism is still unknown.

4.12.1. Antifungal Activity of IONPs on F. solani Radial Mycelium Growth. The antifungal activity of NPs was determined by measuring the colony diameter and the percentage of inhibition of *F. solani* (Figure S9). It was found that as the concentration of NPs increases, the fungi's colony diameter decreased. This method allows us to determine the NP concentration at which the fungal mycelia are completely inhibited from growing. The fungal colony was completely inhibited at 3000 μg/mL. The mycelium diameter of the colony cultured on the plate containing 100, 250, 500, 1000, and 2000 μg/mL of NPs was 7.6, 6.8, 5.5, 4.8, and 2.5 cm, respectively. The results of the experiment support the dose-dependent action of the produced NPs. In 7 days, the untreated plate showed full colony growth to a diameter of 9 cm. The NPs have severely harmed the ultrastructural morphology of the fungal conidia. When fungal spores were exposed to NPs, membrane destabilization occurred due to proteolytic leakage of fungal conidia. The use of NPs result in non-viable spores (Figure 5h). The spores that were not treated, on the other hand, displayed no morphological abnormalities (Figure 5g).

4.12.2. Effect of NPs on F. solani Spore Germination Inhibition. The spore's germination is sensitive to environmental changes as well as abiotic and biotic stress exposure. These stressors have an effect on the cellular integrity of the spores and cause morphological changes that sometimes prevent them from germinating. Our findings indicate that spore germination is completely inhibited at the highest tested concentration of NPs. When spores are treated with 3000 μg/mL of biosynthesized NPs, spore germination is completely inhibited (Figure S10).

5. CONCLUSIONS

In conclusion, green-mediated IONPs were synthesized from the biowaste of the juice processing industry. The synthesis procedure is both economical and environmentally beneficial. Catalysis reaction parameters (neutral pH, absence of photo radiation/ultrasonication, contact time, catalyst amount, peroxide amount) improve the overall scenario of this Fenton-like reaction. The current work's overall output allows for the use of nanocatalysts in wastewater remediation in neutral pH and other practical uses of treated wastewater, such as plant growth. Also, treated wastewater has a positive effect on the biochemical properties of the wheat plant. Physical characterization revealed that cubical shaped Fe_2O_3 NPs with an average size of 42 nm were synthesized. According to FTIR analysis, phytochemicals of LPE play a significant role in the synthesis procedure. According to DLS and ζ potential analysis, NPs are very stable. Synthesized NPs have strong antimicrobial activities and demonstrated significant free-radical scavenging activity against DPPH, which can be attributed to LPE phytochemicals. We believe that our findings will pique people's interest in using high-performance nanocatalysts to reduce pollution. Future work will focus on evaluating this system by employing the real water sample of dye-contaminated areas and detecting the actual intermediates formed during the oxidation process.

https://doi.org/10.1021/acsomega.2c03798
ACS Omega 2022, 7, 44698−44710

■ ASSOCIATED CONTENT

Supporting Information

The Supporting Information is available free of charge at https://pubs.acs.org/doi/10.1021/acsomega.2c03798.

Phytochemical screening of LPE, XRD data of IONPs, proposed mechanism of green synthesis hematite NPs, first-order reaction kinetics for decolorization of MB by Fenton-like reactions, plots of rate constant of first-order reaction, seed germination and seedling vigor evaluation of wheat seedlings, evaluation of biochemical attributes of treated wheat seedlings, bar graph showing zone of inhibition introduced by IONPs, visual representations of proposed mechanisms of antibacterial activity of IONPs, concentration−response curve on DPPH radical scavenging capacity of IONPs synthesized from LPE, PIRG of F. solani under tested concentrations of IONPs, effect of IONPs on inhibition percentage of spore germination of F. solani, DLS of the recovered catalyst after third cycles, and zeta potential of the recovered catalyst after the third cycle, and effect of only hydrogen peroxide on dye degradation (PDF)

■ AUTHOR INFORMATION

Corresponding Author

Mahendra Nath Roy − *Department of Chemistry, University of North Bengal, Darjeeling 734013, India; Department of Chemistry, Alipurduar University, Alipurduar 736122, India;* orcid.org/0000-0002-7380-5526; Email: mahendraroy2002@yahoo.co.in

Authors

Debasmita Das − *Department of Chemistry, University of North Bengal, Darjeeling 734013, India*

Salim Ali − *Department of Chemistry, University of North Bengal, Darjeeling 734013, India*

Biplab Rajbanshi − *Department of Chemistry, University of North Bengal, Darjeeling 734013, India*

Samapika Ray − *Department of Chemistry, University of North Bengal, Darjeeling 734013, India*

Sanjoy Barman − *Department of Chemistry, University of North Bengal, Darjeeling 734013, India*

Divya Chouhan − *Nanobiology and Phytotherapy Laboratory, Department of Botany, University of North Bengal, Siliguri 734013 West Bengal, India*

Md Salman Haydar − *Nanobiology and Phytotherapy Laboratory, Department of Botany, University of North Bengal, Siliguri 734013 West Bengal, India;* orcid.org/0000-0003-4725-8562

Palash Mandal − *Nanobiology and Phytotherapy Laboratory, Department of Botany, University of North Bengal, Siliguri 734013 West Bengal, India*

Kanak Roy − *Department of Chemistry, Alipurduar University, Alipurduar 736122, India*

Vikas Kumar Dakua − *Department of Chemistry, Alipurduar University, Alipurduar 736122, India*

Complete contact information is available at: https://pubs.acs.org/10.1021/acsomega.2c03798

Notes

The authors declare no competing financial interest.

■ ACKNOWLEDGMENTS

The authors gratefully acknowledge the Department of Chemistry and Botany, NBU, for instrumental assistance and biological assay.

■ REFERENCES

(1) Saeed, M.; Muneer, M.; Akram, N.; ul Haq, A.; Afzal, N.; Hamayun, M. Synthesis and characterization of silver loaded alumina and evaluation of its photo catalytic activity on photo degradation of methylene blue dye. *Chem. Eng. Res. Des.* **2019**, *148*, 218−226.

(2) Balcha, A.; Yadav, O. P.; Dey, T. Photocatalytic degradation of methylene blue dye by zinc oxide nanoparticles obtained from precipitation and sol-gel methods. *Environ. Sci. Pollut. Res.* **2016**, *23*, 25485−25493.

(3) Nidheesh, P.; Zhou, M.; Oturan, M. A. An overview on the removal of synthetic dyes from water by electrochemical advanced oxidation processes. *Chemosphere* **2018**, *197*, 210−227.

(4) Salazar, C.; Ridruejo, C.; Brillas, E.; Yáñez, J.; Mansilla, H. D.; Sirés, I. Abatement of the fluorinated antidepressant fluoxetine (Prozac) and its reaction by-products by electrochemical advanced methods. *Appl. Catal.* **2017**, *203*, 189−198.

(5) Peyton, G. R.; Bell, O. J.; Girin, E.; LeFaivre, M. H. Reductive destruction of water contaminants during treatment with hydroxyl radical processes. *Environ. Sci. Technol.* **1995**, *29*, 1710−1712.

(6) Baciocchi, R.; Boni, M. R.; D'Aprile, L. Hydrogen peroxide lifetime as an indicator of the efficiency of 3-chlorophenol Fenton's and N Fenton-like oxidation in soils. *J. Hazard. Mater.* **2003**, *96*, 305−329.

(7) Nogueira, R. F. P.; Oliveira, M. C.; Paterlini, W. C. Simple and fast spectrophotometric determination of H2O2 in photo-Fenton reactions using metavanadate. *Talanta* **2005**, *66*, 86−91.

(8) Jung, Y. S.; Lim, W. T.; Park, J. Y.; Kim, Y. H. Effect of pH on Fenton and Fenton-like oxidation. *Environ. Technol.* **2009**, *30*, 183−190.

(9) Jain, B.; Singh, A. K.; Kim, H.; Lichtfouse, E.; Sharma, V. K. Treatment of organic pollutants by homogeneous and heterogeneous Fenton reaction processes. *Environ. Chem. Lett.* **2018**, *16*, 947−967.

(10) Yang, S.; He, H.; Wu, D.; Chen, D.; Liang, X.; Qin, Z.; Fan, M.; Zhu, J.; Yuan, P. Decolorization of methylene blue by heterogeneous Fenton reaction using Fe3− xTixO4 (0≤ x≤ 0.78) at neutral pH values. *Appl. Catal. B Environ.* **2009**, *89*, 527−535.

(11) Karpagavinayagam, P.; Vedhi, C. Green synthesis of iron oxide nanoparticles using Avicennia marina flower extract. *Vacuum* **2019**, *160*, 286−292.

(12) Demirezen, D. A.; Yıldız, Y. Ş.; Yılmaz, Ş.; Yılmaz, D. D. Green synthesis and characterization of iron oxide nanoparticles using Ficus carica (common fig) dried fruit extract. *J. Biosci. Bioeng.* **2019**, *127*, 241−245.

(13) Jassal, V.; Shanker, U.; Gahlot, S. Green synthesis of some iron oxide nanoparticles and their interaction with 2-amino, 3-amino and 4-aminopyridines. *Mater. Today* **2016**, *3*, 1874−1882.

(14) Kanagasubbulakshmi, S.; Kadirvelu, K. Green synthesis of iron oxide nanoparticles using Lagenaria siceraria and evaluation of its antimicrobial activity. *Def. Life Sci. J.* **2017**, *2*, 422−427.

(15) Arularasu, M.; Devakumar, J.; Rajendran, T. An innovative approach for green synthesis of iron oxide nanoparticles: Characterization and its photocatalytic activity. *Polyhedron* **2018**, *156*, 279−290.

(16) Muthukumar, H.; Matheswaran, M. Amaranthus spinosus leaf extract mediated FeO nanoparticles: physicochemical traits, photocatalytic and antioxidant activity. *ACS Sustainable Chem. Eng.* **2015**, *3*, 3149−3156.

(17) Beheshtkhoo, N.; Kouhbanani, M. A. J.; Savardashtaki, A.; Amani, A. M.; Taghizadeh, S. Green synthesis of iron oxide nanoparticles by aqueous leaf extract of Daphne mezereum as a novel dye removing material. *Appl. Phys. A* **2018**, *124*, 363.

(18) Wei, Y.; Fang, Z.; Zheng, L.; Tan, L.; Tsang, E. P. Green synthesis of Fe nanoparticles using Citrus maxima peels aqueous extracts. *Mater. Lett.* **2016**, *185*, 384−386.

(19) Patiño-Ruiz, D.; Sánchez-Botero, L.; Tejeda-Benitez, L.; Hinestroza, J.; Herrera, A. Green synthesis of iron oxide nanoparticles using Cymbopogon citratus extract and sodium carbonate salt: Nanotoxicological considerations for potential environmental applications. *Eviron. Nanotechnol. Monit. Manag.* **2020**, *14*, 100377.
(20) Jahan, I.; Işildak, İ. Lemon Peel Extract for Synthesizing Non-Toxic Silver Nanoparticles through One-Step Microwave-Accelerated Scheme. *KSU J. Agric. Nat.* **2021**, *24*, 1−10.
(21) Dutta, T.; Ghosh, N. N.; Das, M.; Adhikary, R.; Mandal, V.; Chattopadhyay, A. P. Green synthesis of antibacterial and antifungal silver nanoparticles using Citrus limetta peel extract: Experimental and theoretical studies. *J. Environ. Chem. Eng.* **2020**, *8*, 104019.
(22) Rufus, A.; Sreeju, N.; Philip, D. Synthesis of biogenic hematite (α-Fe 2 O 3) nanoparticles for antibacterial and nanofluid applications. *RSC Adv.* **2016**, *6*, 94206−94217.
(23) Muthukumar, H.; Chandrasekaran, N. I.; Naina Mohammed, S. N.; Pichiah, S.; Manickam, M. Iron oxide nano-material: physicochemical traits and in vitro antibacterial propensity against multidrug resistant bacteria. *J. Ind. Eng. Chem.* **2017**, *45*, 121−130.
(24) El-Bassuony, A. A. H.; Abdelsalam, H. K. Impacts of hematite, bunsenite and maghemite impurities on the physical and antimicrobial properties of silver nanoparticles. *Eur. Phys. J. Plus* **2020**, *135*, 64.
(25) Jamzad, M.; Kamari Bidkorpeh, M. Green synthesis of iron oxide nanoparticles by the aqueous extract of Laurus nobilis L. leaves and evaluation of the antimicrobial. *J. Nanostruct. Chem.* **2020**, *10*, 193−201.
(26) Rajendran, K.; Sen, S.; Suja, G.; Senthil, S. L.; Kumar, T. V. Evaluation of cytotoxicity of hematite nanoparticles in bacteria and human cell lines. *Colloids Surf., B* **2017**, *157*, 101−109.
(27) Selvaraj, R.; Pai, S.; Murugesan, G.; Pandey, S.; Bhole, R.; Gonsalves, D.; Varadavenkatesan, T.; Vinayagam, R. Green synthesis of magnetic α−Fe2O3 nanospheres using Bridelia retusa leaf extract for Fenton-like degradation of crystal violet dye. *Appl. Nanosci.* **2021**, *11*, 2227−2234.
(28) Itelima, J.; Nwokedi, V.; Ogbonna, A.; Nyam, M.*Phytochemical Screening and Antimicrobial Activity Evaluation of Aqueous and Ethanolic Extracts of the Leaf of Azadirachta Indica Juss (neem) on Some Microorganisms*, 2016.
(29) Miri, A.; Mahabbati, F.; Najafidoust, A.; Miri, M. J.; Sarani, M. Nickel oxide nanoparticles: biosynthesized, characterization and photocatalytic application in degradation of methylene blue dye. *Inorg. Nano-Met. Chem.* **2022**, *52*, 122−131.
(30) Ullah, R.; Dutta, J. Photocatalytic degradation of organic dyes with manganese-doped ZnO nanoparticles. *J. Hazard. Mater.* **2008**, *156*, 194−200.
(31) Das, D.; Haydar, M. S.; Mandal, P. Impact of physical attributes on proficient phytosynthesis of silver nanoparticles using extract of fresh mulberry leaves: characterization, stability and bioactivity assessment. *J. Inorg. Organomet. Polym. Mater.* **2021**, *31*, 1527−1548.
(32) Dananjaya, S.; Erandani, W.; Kim, C.-H.; Nikapitiya, C.; Lee, J.; De Zoysa, M. Comparative study on antifungal activities of chitosan nanoparticles and chitosan silver nano composites against Fusarium oxysporum species complex. *Int. J. Biol. Macromol.* **2017**, *105*, 478−488.
(33) Ahmed, A.Chitosan and silver nanoparticles as control agents of some Faba bean spot diseases. *J. Plant Pathol. Microbiol.***2017**, *8*, DOI: 10.4172/2157-7471.1000421.
(34) Lakshminarayanan, S.; Shereen, M. F.; Niraimathi, K.; Brindha, P.; Arumugam, A. One-pot green synthesis of iron oxide nanoparticles from Bauhinia tomentosa: Characterization and application towards synthesis of 1, 3 diolein. *Sci. Rep.* **2021**, *11*, 8643.
(35) Çitoğlu, S.; Coşkun, Ö. D.; Tung, L. D.; Onur, M. A.; Thanh, N. T. K. DMSA-coated cubic iron oxide nanoparticles as potential therapeutic agents. *Nanomedicine* **2021**, *16*, 925−941.
(36) Shah, R.; Eldridge, D.; Palombo, E.; Harding, I.Optimisation and stability assessment of solid lipid nanoparticles using particle size and zeta potential. *J. Phys. Sci.***2014**, *25*.
(37) Taghavi Fardood, S.; Ramazani, A.; Golfar, Z.; Woo Joo, S. Green Synthesis of α-Fe2O (hematite) Nanoparticles using Tragacanth Gel. *JACR* **2017**, *11*, 19−27.
(38) Bhuyar, P.; Rahim, M. H. A.; Sundararaju, S.; Ramaraj, R.; Maniam, G. P.; Govindan, N. Synthesis of silver nanoparticles using marine macroalgae Padina sp. and its antibacterial activity towards pathogenic bacteria. *Beni-Suef Univ. J. Basic Appl. Sci.* **2020**, *9*, 3.
(39) Tharani, K.; Nehru, L. Synthesis and characterization of iron oxide nanoparticle by precipitation method. *Int. J. Adv. Res. Phys. Sci.* **2015**, *2*, 47−50.
(40) Parhizkar, J.; Habibi, M. H. Synthesis, characterization and photocatalytic properties of Iron oxide nanoparticles synthesized by sol-gel autocombustion with ultrasonic irradiation. *Nanochem. Res.* **2017**, *2*, 166−171.
(41) Archana, V.; Joseph Prince, J.; Kalainathan, S. Simple one-step leaf extract-assisted preparation of α-Fe2O3 nanoparticles, physicochemical properties, and its sunlight-driven photocatalytic activity on methylene blue dye degradation. *J. Nanomater.* **2021**, *2021*, 1.
(42) Jeyaseelana, S. J.; Parasuramana, K.; Jeyakumarb, S. J.; Jothibasb, M.*Structural, Optical and Magnetic Properties of Fe_2O_3 Synthesis via Sol-Gel Technique*, 2019.
(43) Atul; Kumar, M.; Sharma, A.; Maurya, I. K.; Thakur, A.; Kumar, S. Synthesis of ultra small iron oxide and doped iron oxide nanostructures and their antimicrobial activities. *J. Taibah Univ. Sci.* **2019**, *13*, 280−285.
(44) Bozkurt, G. Synthesis and Characterization of α-Fe2O3 Nanoparticles by Microemulsion Method. *Erzincan University Journal of Science and Technology* **2020**, *13*, 890−897.
(45) Pal, B.; Sharon, M. Preparation of iron oxide thin film by metal organic deposition from Fe (III)-acetylacetonate: a study of photocatalytic properties. *Thin Solid Films* **2000**, *379*, 83−88.
(46) Darezereshki, E. One-step synthesis of hematite (α-Fe2O3) nano-particles by direct thermal-decomposition of maghemite. *Mater. Lett.* **2011**, *65*, 642−645.
(47) Khalil, A. T.; Ovais, M.; Ullah, I.; Ali, M.; Shinwari, Z. K.; Maaza, M. Biosynthesis of iron oxide (Fe2O3) nanoparticles via aqueous extracts of Sageretia thea (Osbeck.) and their pharmacognostic properties. *Green Chem. Lett. Rev.* **2017**, *10*, 186−201.
(48) Hwang, S.; Umar, A.; Dar, G.; Kim, S.; Badran, R. Synthesis and characterization of iron oxide nanoparticles for phenyl hydrazine sensor applications. *Sens. Lett.* **2014**, *12*, 97−101.
(49) Apte, S.; Naik, S.; Sonawane, R.; Kale, B.; Baeg, J. Synthesis of nanosize-necked structure α-and γ-Fe2O3 and its photocatalytic activity. *J. Am. Ceram. Soc.* **2007**, *90*, 412−414.
(50) Coates, J.; Meyers, R.*Encyclopedia of Analytical Chemistry*; Wiley: Chichester, U.K., 2000; pp 10815−10837.
(51) Song, L.; Zhang, S.; Chen, B.; Ge, J.; Jia, X. A hydrothermal method for preparation of α-Fe2O3 nanotubes and their catalytic performance for thermal decomposition of ammonium perchlorate. *Colloids Surf. A Physicochem. Eng. Asp.* **2010**, *360*, 1−5.
(52) Mahanty, S.; Bakshi, M.; Ghosh, S.; Chatterjee, S.; Bhattacharyya, S.; Das, P.; Das, S.; Chaudhuri, P. Green synthesis of iron oxide nanoparticles mediated by filamentous fungi isolated from Sundarban mangrove ecosystem, India. *Bionanoscience* **2019**, *9*, 637−651.
(53) Demir, A.; Topkaya, R.; Baykal, A. Green synthesis of superparamagnetic Fe3O4 nanoparticles with maltose: its magnetic investigation. *Polyhedron* **2013**, *65*, 282−287.
(54) Yew, Y. P.; Shameli, K.; Miyake, M.; Ahmad Khairudin, N. B. B. A.; Mohamad, S. E. B.; Naiki, T.; Lee, K. X. Green biosynthesis of superparamagnetic magnetite Fe3O4 nanoparticles and biomedical applications in trgeted anticancer drug delivery system: A review. *Arab. J. Chem.* **2020**, *13*, 2287−2308.
(55) Pugazhenthiran, N.; Anandan, S.; Kathiravan, G.; Udaya Prakash, N. K.; Crawford, S.; Ashokkumar, M. Microbial synthesis of silver nanoparticles by Bacillus sp. *J. Nanoparticle Res.* **2009**, *11*, 1811−1815.
(56) Yadav, V. K.; Ali, D.; Khan, S. H.; Gnanamoorthy, G.; Choudhary, N.; Yadav, K. K.; Thai, V. N.; Hussain, S. A.; Manhrdas,

https://doi.org/10.1021/acsomega.2c03798
ACS Omega 2022, 7, 44698−44710

S. Synthesis and characterization of amorphous iron oxide nanoparticles by the sonochemical method and their application for the remediation of heavy metals from wastewater. *Nanomaterials* **2020**, *10*, 1551.
(57) Hua, J.; Gengsheng, J. Hydrothermal synthesis and characterization of monodisperse α-Fe2O3 nanoparticles. *Mater. Lett.* **2009**, *63*, 2725−2727.
(58) Almeida, T. P.; Fay, M.; Zhu, Y.; Brown, P. D. Process map for the hydrothermal synthesis of α-Fe2O3 nanorods. *J. Phys. Chem. C* **2009**, *113*, 18689−18698.
(59) Ahmmad, B.; Leonard, K.; Shariful Islam, M. S.; Kurawaki, J.; Muruganandham, M.; Ohkubo, T.; Kuroda, Y. Green synthesis of mesoporous hematite (α-Fe2O3) nanoparticles and their photocatalytic activity. *Adv. Powder Technol.* **2013**, *24*, 160−167.
(60) Naz, S.; Islam, M.; Tabassum, S.; Fernandes, N. F.; Carcache de Blanco, E. J. C.; Zia, M. Green synthesis of hematite (α-Fe2O3) nanoparticles using Rhus punjabensis extract and their biomedical prospect in pathogenic diseases and cancer. *J. Mol. Struct.* **2019**, *1185*, 1−7.
(61) Nagajyothi, P.; Pandurangan, M.; Kim, D. H.; Sreekanth, T.; Shim, J. Green synthesis of iron oxide nanoparticles and their catalytic and in vitro anticancer activities. *J. Clust. Sci.* **2017**, *28*, 245−257.
(62) Mariam, A. A.; Kashif, M.; Arokiyaraj, S.; Bououdina, M.; Sankaracharyulu, M.; Jayachandran, M.; Hashim, U. Bio-synthesis of NiO and Ni nanoparticles and their characterization. *Dig. J. Nanomater. Biostructures* **2014**, *9*, 1007−1019.
(63) Thirumamagal, R.; Irshad Ahamed, S.; Nivetha, S.; Saravanakkumar, D.; Ayeshamariam, A. Comparative morphological studies on NiO, CoO and Fe2O3 nanoparticles. *J. Powder Metall. Min.* **2017**, *6*, 2.
(64) Kannan, K.; Radhika, D.; Reddy, K. R.; Raghu, A. V.; Sadasivuni, K. K.; Palani, G.; Gurushankar, K. Gd3+ and Y3+ co-doped mixed metal oxide nanohybrids for photocatalytic and antibacterial applications. *Nano express* **2021**, *2*, 010014.
(65) Shahwan, T.; Erten, H. Thermodynamic parameters of Cs+ sorption on natural clays. *J. Radioanal. Nucl. Chem.* **2002**, *253*, 115−120.
(66) Ayodamope, E. O. Oxidative degradation of methylene blue using Fenton reagent. *Int. J. Sci. Eng. Res.* **2015**, *6*, 984−995.
(67) Alayli, A.; Nadaroglu, H.; Turgut, E. Nanobiocatalyst beds with Fenton process for removal of methylene blue. *Appl. Water Sci.* **2021**, *11*, 32.
(68) Briton, B. G. H.; Duclaux, L.; Richardson, Y.; Yao, K. B.; Reinert, L.; Soneda, Y. Effectiveness of the dispersion of iron nanoparticles within micropores and mesopores of activated carbon for Rhodamine B removal in wastewater by the heterogeneous Fenton process. *Appl. Water Sci.* **2019**, *9*, 166.
(69) Abhilasha, J.; Ashma, A.; Marazban, K. A greener approach for the degradation of dye methylene blue by organic additive catalysed photo-fenton process. *J. Chil. Chem. Soc.* **2016**, *61*, 3043−3048.
(70) Fathinia, S.; Fathinia, M.; Rahmani, A. A.; Khataee, A. Preparation of natural pyrite nanoparticles by high energy planetary ball milling as a nanocatalyst for heterogeneous Fenton process. *Appl. Surf. Sci.* **2015**, *327*, 190−200.
(71) Luo, Y.; Guo, W.; Ngo, H. H.; Nghiem, L. D.; Hai, F. I.; Zhang, J.; Liang, S.; Wang, X. C. A review on the occurrence of micropollutants in the aquatic environment and their fate and removal during wastewater treatment. *Sci. Total Environ.* **2014**, *473*−*474*, 619−641.
(72) Bishnoi, S.; Kumar, A.; Selvaraj, R. Facile synthesis of magnetic iron oxide nanoparticles using inedible Cynometra ramiflora fruit extract waste and their photocatalytic degradation of methylene blue dye. *Mater. Res. Bull.* **2018**, *97*, 121−127.
(73) Singh, A.; Bhati, A.; Khare, P.; Tripathi, K. M.; Sonkar, S. K. Soluble graphene nanosheets for the sunlight-induced photodegradation of the mixture of dyes and its environmental assessment. *Sci. Rep.* **2019**, *9*, 1−12.
(74) Anchan, S.; Pai, S.; Sridevi, H.; Varadavenkatesan, T.; Vinayagam, R.; Selvaraj, R. Biogenic synthesis of ferric oxide nanoparticles using the leaf extract of Peltophorum pterocarpum and their catalytic dye degradation potential. *Biocatal. Agric. Biotechnol.* **2019**, *20*, 101251.
(75) Chen, W.; Yang, X.; Huang, J.; Zhu, Y.; Zhou, Y.; Yao, Y.; Li, C. Iron oxide containing graphene/carbon nanotube based carbon aerogel as an efficient E-Fenton cathode for the degradation of methyl blue. *Electrochim. Acta* **2016**, *200*, 75−83.
(76) Wang, H.; Huang, Y. Prussian-blue-modified iron oxide magnetic nanoparticles as effective peroxidase-like catalysts to degrade methylene blue with H2O2. *J. Hazard. Mater.* **2011**, *191*, 163−169.
(77) Ren, B.; Xu, Y.; Zhang, C.; Zhang, L.; Zhao, J.; Liu, Z. Degradation of methylene blue by a heterogeneous Fenton reaction using an octahedron-like, high-graphitization, carbon-doped Fe2O3 catalyst. *J. Taiwan Inst. Chem. Eng.* **2019**, *97*, 170−177.
(78) Ashraf, G. A.; Rasool, R. T.; Hassan, M.; Zhang, L.; Guo, H. Heterogeneous catalytic activation of BaCu-based M-hexaferrite nanoparticles for methylene blue degradation under photo-Fenton-like system. *Mol. Catal.* **2021**, *505*, 111501.
(79) Kalam, A.; Al-Sehemi, A. G.; Assiri, M.; Du, G.; Ahmad, T.; Ahmad, I.; Pannipara, M. Modified solvothermal synthesis of cobalt ferrite (CoFe2O4) magnetic nanoparticles photocatalysts for degradation of methylene blue with H2O2/visible light. *Results Phys.* **2018**, *8*, 1046−1053.
(80) Yang, B.; Tian, Z.; Zhang, L.; Guo, Y.; Yan, S. Enhanced heterogeneous Fenton degradation of Methylene Blue by nanoscale zero valent iron (nZVI) assembled on magnetic Fe3O4/reduced graphene oxide. *J. Colloid Interface Sci.* **2015**, *5*, 101−111.
(81) Hammad, M.; Fortugno, P.; Hardt, S.; Kim, C.; Salamon, S.; Schmidt, T. C.; Wende, H.; Schulz, C.; Wiggers, H. Large-scale synthesis of iron oxide/graphene hybrid materials as highly efficient photo-Fenton catalyst for water remediation. *Environ. Technol. Innovat.* **2021**, *21*, 101239.
(82) Abid, M. A.; Kadhim, D. A. Novel comparison of iron oxide nanoparticle preparation by mixing iron chloride with henna leaf extract with and without applied pulsed laser ablation for methylene blue degradation. *J. Environ. Chem. Eng.* **2020**, *8*, 104138.
(83) Abid, M. A.; Abid, D. A.; Aziz, W. J.; Rashid, T. M. Iron oxide nanoparticles synthesized using garlic and onion peel extracts rapidly degrade methylene blue dye. *Phys. B Condens. Matter* **2021**, *622*, 413277.
(84) Wanakai, S. I.; Kareru, P. G.; Makhanu, D. S.; Madivoli, E. S.; Maina, E. G.; Nyabola, A. O. Catalytic degradation of methylene blue by iron nanoparticles synthesized using Galinsoga parviflora, Conyza bonariensis and Bidens pilosa leaf extracts. *SN Appl. Sci.* **2019**, *1*, 1148.
(85) Priac, A.; Badot, P.-M.; Crini, G. Treated wastewater phytotoxicity assessment using Lactuca sativa: focus on germination and root elongation test parameters. *C. R. Biol.* **2017**, *340*, 188−194.
(86) Parvin, F.; Ferdaus, Z.; Tareq, S. M.; Choudhury, T. R.; Islam, J. M.; Khan, M. A. Effect of gamma-irradiated textile effluent on plant growth. *Int. J. Recycl. Org. Waste Agric.* **2015**, *4*, 23−30.
(87) Parvin, F.; Nayna, O. K.; Tareq, S. M.; Rikta, S. Y.; Kamal, A. K. Facile synthesis of iron oxide nanoparticle and synergistic effect of iron nanoparticle in the presence of sunlight for the degradation of DOM from textile wastewater. *Appl. Water Sci.* **2018**, *8*, 73.
(88) Bhat, S. A.; Zafar, F.; Mondal, A. H.; Kareem, A.; Mirza, A. U.; Khan, S.; Mohammad, A.; Haq, Q. M.; Nishat, N. Photocatalytic degradation of carcinogenic Congo red dye in aqueous solution, antioxidant activity and bactericidal effect of NiO nanoparticles. *J. Iran. Chem. Soc.* **2020**, *17*, 215−227.
(89) Bhattacharya, K.; Gogoi, B.; Buragohain, A.; Deb, P. Fe2O3/C nanocomposites having distinctive antioxidant activity and hemolysis prevention efficiency. *Mater. Sci. Eng. C* . **2014**, *42*, 595−600.
(90) Olapade, O. A.; Depas, M. M.; Jensen, E. T.; McLellan, S. L. Microbial communities and fecal indicator bacteria associated with Cladophora mats on beach sites along Lake Michigan shores. *Appl. Environ. Microbiol.* **2006**, *72*, 1932−1938.

https://doi.org/10.1021/acsomega.2c03798
ACS Omega 2022, 7, 44698−44710

(91) Kareem, Z. H.; Shareef, H. K.; Alkaim, A. F. Evaluation of antibacterial activity of Fê sub 2 Ô sub 3 nanoparticles against Shigella dysenteriae. *J. Pharm. Sci. Res.* **2018**, *10*, 1980−1982.
(92) Arakha, M.; Pal, S.; Samantarrai, D.; Panigrahi, T. K.; Mallick, B. C.; Pramanik, K.; Mallick, B.; Jha, S. Antimicrobial activity of iron oxide nanoparticle upon modulation of nanoparticle-bacteria interface. *Sci. Rep.* **2015**, *5*, 14813.
(93) Sundara Selvam, P. S.; Govindan, S.; Perumal, B.; Kandan, V. Screening of In Vitro Antibacterial Property of Hematite (α-Fe2O3) Nanoparticles: A Green Approach. *Iran. J. Sci. Technol. Trans. A-Science* **2021**, *45*, 177−187.
(94) Zare, E.; Pourseyedi, S.; Khatami, M.; Darezereshki, E. Simple biosynthesis of zinc oxide nanoparticles using nature's source, and it's in vitro bio-activity. *J. Mol. Struct.* **2017**, *1146*, 96−103.
(95) Ruiz-Romero, P.; Valdez-Salas, B.; González-Mendoza, D.; Mendez-Trujillo, V. Antifungal effects of silver phytonanoparticles from Yucca shilerifera against strawberry soil-borne pathogens: Fusarium solani and Macrophomina phaseolina. *Mycobiology* **2018**, *46*, 47−51.
(96) Boxi, S. S.; Mukherjee, K.; Paria, S. Ag doped hollow TiO2 nanoparticles as an effective green fungicide against Fusarium solani and Venturia inaequalis phytopathogens. *Nanotechnology* **2016**, *27*, 085103.

https://doi.org/10.1021/acsomega.2c03798
ACS Omega 2022, 7, 44698−44710